FULL PAPER

Photocatalytic Water Splitting

ADVANCED
OPTICAL
MATERIALS

www.advopticalmat.d

Phase and Defect Engineering of MoS$_2$ Stabilized in Periodic TiO$_2$ Nanoporous Film for Enhanced Solar Water Splitting

Limin Guo, Caifu Zhong, Li Shi, Licheng Ju, Xiaohui Wang, Daquan Yang, Ke Bi,* Yanan Hao,* and Yang Yang*

Phase and defect engineering of the heterostructured MoS$_2$@TiO$_2$ nanoporous film is investigated to achieve a broad solar spectrum light absorption and high solar water splitting efficiency. The phase transition from the semiconducting 2H-MoS$_2$ to the metallic 1T-MoS$_2$ is achieved by a hydrothermal exfoliation treatment. Experimental studies elucidate that the solar water splitting activity is greatly improved by forming 1T-MoS$_2$ along with increasing S-vacancies because of the significantly enhanced surface plasmon resonance. The mixed-phase MoS$_2$@TiO$_2$ film shows a high H$_2$ yield rate of 308 µmol h^{-1} cm^{-2} and long-term durability for 30 h, which is superior to the state-of-the-art catalysts for solar water splitting. This study offers a universal and efficient avenue to rationalize the plasmonic catalysts for solar water splitting and other energy and environmental applications.

1. Introduction

Hydrogen (H$_2$) generation by means of solar water splitting has been extensively exploited to meet the ever-growing energy demands and to address the environmental concerns.[1]

Dr. L. Guo, Prof. D. Yang, Prof. K. Bi, Dr. Y. Hao
State Key Laboratory of Information Photonics and Optical
Communications
School of Science
Beijing University of Posts and Telecommunications
Beijing 100876, China
E-mail: bike@bupt.edu.cn; hyn@bupt.edu.cn
Dr. L. Guo, Dr. L. Shi, L. Ju, Prof. Y. Yang
NanoScience Technology Center
Department of Materials Science and Engineering
University of Central Florida
4000 Central Florida Blvd., Orlando, FL 32816, USA
E-mail: Yang.Yang@ucf.edu
Dr. C. Zhong
Energy Research Institute
National Development and Reform Commission
Beijing 100038, China
Prof. X. Wang
State Key Laboratory of New Ceramics and Fine Processing
Department of Materials Science and Engineering
Tsinghua University
Beijing 100084, China

The ORCID identification number(s) for the author(s) of this article
can be found under https://doi.org/10.1002/adom.201801403.

Bandgap engineering of semiconductor catalysts has therefore been investigated for decades to achieve to an ultraviolet–visible (UV–vis) light absorption for efficient solar-to-H$_2$ (STH) conversion.[2] Unfortunately, a single semiconductor alone can barely meet the requirements for water photolysis due to the limited light absorption in a broad solar spectrum and short carrier lifetime. For example, TiO$_2$ or ZnO can only be excited in the UV region, which occupies less than 5% in the solar spectrum.[3] Meanwhile, some narrow-bandgap semiconductors (e.g., CdS and Fe$_2$O$_3$) absorb the visible light, however, the diminished carrier lifetime and inevitable recombination limit their photocatalytic applications.[4] To overcome these obstacles, the hybrid catalysts have been designed by integrating two or more semiconductors with proper band alignment.[4] However, the free electron exhaust and catalytic performance degradation caused by the interplay of different components turn out to be considerable. In addition, the utilization of near-infrared (NIR, 45% of the solar energy) light is still very challenging in the hybrid catalysts.[5] It is very urgent to develop stable catalysts that can absorb photons in a broad solar light spectrum covering UV–vis–NIR wavelength.

Plasmonic nanostructures of noble metals (e.g., Au and Ag) have been recently explored as promising candidates for solar energy harvesting and solar H$_2$ production due to the localized surface plasmon resonance (LSPR).[3b,6,7] However, the high cost and poor stability limit the large-scale and long-term utilization of theses plasmonic catalysts. Most recently, some nonprecious metals or nonmetallic nanocrystals (NCs) have been newly burgeoned as plasmonic nanostructures, including metal oxides (WO$_{3-x}$), metal chalcogenides (Cu$_{2-x}$S), and graphene.[5,8] Surface defects in the crystal lattice are demonstrated to be indispensable for the free carrier vibration in these materials, leading to LSPR. Most impressively, their intrinsic light absorption is still retained in addition to the resonant photon capture.[8] Yamashita et al. reported an extensive optical response in the visible light and an enhanced H$_2$ yield due to the oxygen vacancies in the W$_{18}$O$_{49}$/g-C$_3$N$_4$ plasmonic catalyst.[5] Plasmonic resonance was also detected on the boundaries of nanoscale graphene and could even be engineered by the number of defects.[9] Moreover, a distinctive noble metal-like plasmonic

**ADVANCED
SCIENCE NEWS**
www.advancedsciencenews.com

**ADVANCED
OPTICAL
MATERIALS**
www.advopticalmat.de

resonance, visible light absorption, and efficient solar H_2 evolution have been elucidated on MoS_2 nanoclusters in the latest research works.[10–13]

The polymorphic MoS_2 typically has trigonal prismatic phase (semiconducting 2H-phase), octahedral phase (metallic 1T-phase), and distorted 1T-phase (semi-metallic 1T'-phase).[14] For decades, phase-/defect-engineering (e.g., S-vacancies) of MoS_2 has been extensively investigated for electrocatalytic H_2 evolution reaction (HER).[10,15] The number of MoS_2 edges, the density of S-vacancies (V_S), and the phase compositions, are considered as crucial factors to adjust the catalytic activity. However, the effects of phase-/defect-engineering on the plasmonic catalysis of MoS_2 are not yet well understood. The origins of LSPR primarily rely on the induced electromagnetic (EM) field enhancement in the plasmonic catalysts, which depends on the free carrier concentrations of the plasmonic materials and the dielectric constants of the surrounding media according to the Drude model.[6,8] Therefore, the size, shape, defect concentration, and polymorph of the plasmonic MoS_2 play equal roles in determining the LSPR and catalytic activity.

Herein, we develop a heterostructured catalyst consisting of MoS_2 nanoflakes (NFs) embedded in the periodic TiO_2 nanocavities (denoted as $MoS_2@TiO_2$) to explore the effects of phase-/defect-engineering on the plasmonic solar water splitting.

Subsequently, well-immobilized and partially 1T-phased MoS_2 NFs were obtained by a hydrothermal treatment in $NaBH_4$ solution. Such partially 1T-phased $MoS_2@TiO_2$ shows an enhanced solar energy harvesting in a broad UV–vis–NIR light spectrum, exhibiting an extraordinary H_2 yield of 308 µmol h^{-1} cm^{-2}, which is superior to the state-of-the-art plasmonic catalysts. Experimental studies reveal that the content of 1T-MoS_2 and the concentration of V_S play crucial roles in improving the solar H_2 evolution.

2. Results and Discussion

The synthetic process of the $MoS_2@TiO_2$ catalyst is schematically illustrated in **Figure 1**a (more details in the Supporting Information). Periodic honeycomb-shaped TiO_2 nanocavity arrays with an average pore size of 50 nm and a wall thickness of 10 nm were obtained by anodization (Figure S1a,b, Supporting Information). 30 nm of Mo was deposited on the anodized TiO_2 nanocavities by e-Beam evaporation, resulting in an obvious cavity wall thickening from 10 to 20 nm (Figure S1c, Supporting Information). After sulfurization treatment at 400 °C for 10 min, the deposited Mo was converted to MoS_2 with a significant shrink of pore size (Figure S2a, Supporting Information). Transmission electron microscopy (TEM) images of $MoS_2@TiO_2$
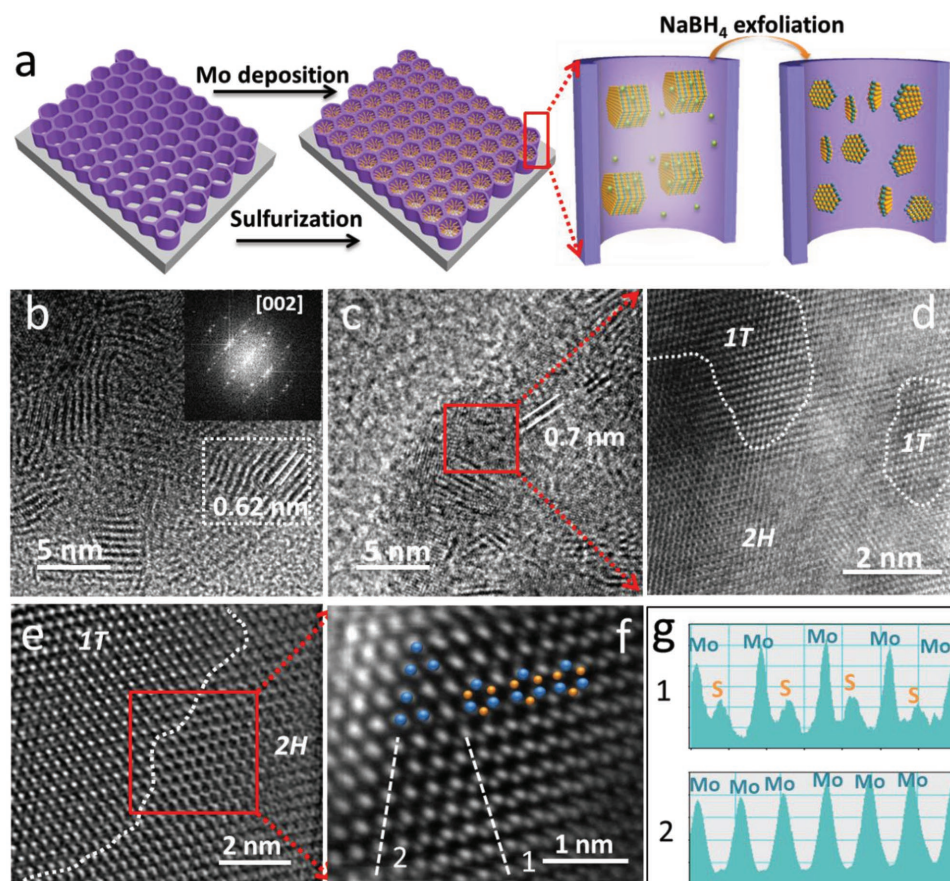

Figure 1. a) Schematic illustration of the fabrication process of $MoS_2@TiO_2$. b,c) TEM images of the pristine $MoS_2@TiO_2$ and $MoS_2@TiO_2$-140, respectively. d) HRTEM image and e,f) atomic-resolution HAADF-STEM image of $MoS_2@TiO_2$-140 with the corresponding inverse FFT image converted from the marked red region. g) Brightness profiles along the dotted lines in inset (f).

**ADVANCED
SCIENCE NEWS**

www.advancedsciencenews.com

**ADVANCED
OPTICAL
MATERIALS**

www.advopticalmat.de

show a highly-ordered 3D lamination of MoS_2 NFs in the TiO_2 nanocavities (Figure 1b; Figure S3a,b, Supporting Information). These MoS_2 NFs are composed of less than ten stacking layers. And part of the MoS_2 nanoflakes stand vertically on the TiO_2 surface or contact with nanocavity walls in a big intersection angle (Figure S3b,c, Supporting Information). High-resolution TEM (HRTEM) images reveal that the fringe spacing of the obtained MoS_2 NFs is about 0.62 nm (Figure 1b). Selected area electron diffraction (SAED) pattern (the inset in Figure 1b) matches well with the MoS_2 (002) planes. Energy dispersive X-ray spectrometry (EDS) mapping (Figure S4, Supporting Information) further demonstrates the immobilized MoS_2 NFs in the TiO_2 nanocavities, forming seamless connections at the MoS_2/TiO_2 interfaces (Figure S4, Supporting Information).

The phase engineering of MoS_2 NFs was carried out by a hydrothermal treatment in 0.1×10^{-3} M $NaBH_4$ solution with a controlled temperature in a range of 140–200 °C. In the following discussion, the samples treated at different temperatures are labeled as $MoS_2@TiO_2$-T, where T represents the hydrothermal temperature. No morphology damage can be identified by the scanning electron microscopy (SEM) observation of the hydrothermally treated samples (Figure S2b–e, Supporting Information), indicating a well-preserved nanostructure. The HRTEM images of $MoS_2@TiO_2$-140 (Figure 1c,d, Supporting Information) show that the size and stacking layer number of MoS_2 NFs decrease to 5 nm and 3–5 layers, respectively, after hydrothermal treatment. Moreover, the layer spacing expands to 0.7 nm due to the generation of MoS_2-H during exfoliation (the intercalated H atoms come from $NaBH_4$).[10,16]

It appears that a slight dissolution of MoS_2 happens in the hydrothermal treatment, which was confirmed from the disordered MoS_2 edges. Atomic-resolution high angle annular dark-field scanning TEM (HAADF-STEM) was used to investigate the ultrathin MoS_2 NFs (Figure 1e). As demonstrated in the red square region of Figure 1e, the honeycomb-like patterns (right side) are observed, consistent with the previously reported 2H-MoS_2.[13b] Meanwhile, some trigonal patterns (octahedral coordination) belonging to the 1T-MoS_2 are also observed at the top left corner of the red square.[13b] The locations of Mo and S atoms are distinguished from the brightness profiles (Figure 1f; Figure S3d, Supporting Information) generated from the inverse fast Fourier transform (FFT)-filtered image of Figure 1e, thus proving the coexistence of 1T-MoS_2 and 2H-MoS_2. The linear brightness profiles along two dotted lines (1, 2) in Figure 1f display a regular arrangement of Mo and S atoms in the 2H- and 1T-MoS_2, respectively, with clear Z (atomic number) contrast (Figure 1g). X-ray diffraction (XRD, Figure S5, Supporting Information) patterns of $MoS_2@TiO_2$ show diffraction peaks of both Ti substrate (PDF Card No.: 44-1294) and anatase TiO_2 (PDF Card No.: 73-1765).[17] A broad peak corresponding to an interlayer d-spacing of MoS_2 (002) facets is identified at 14.48° in the sample before hydrothermal treatment.[18] On the contrary, this diffraction peak disappears after hydrothermal treatment, inferring that the long-range stacking order of the MoS_2 layers along the c-axis is destroyed.

The phase transition of MoS_2 under different hydrothermal temperatures (140, 160, 180 °C) was investigated by the HAADF-STEM (**Figure 2**a–c). The 1T-MoS_2 (green color)
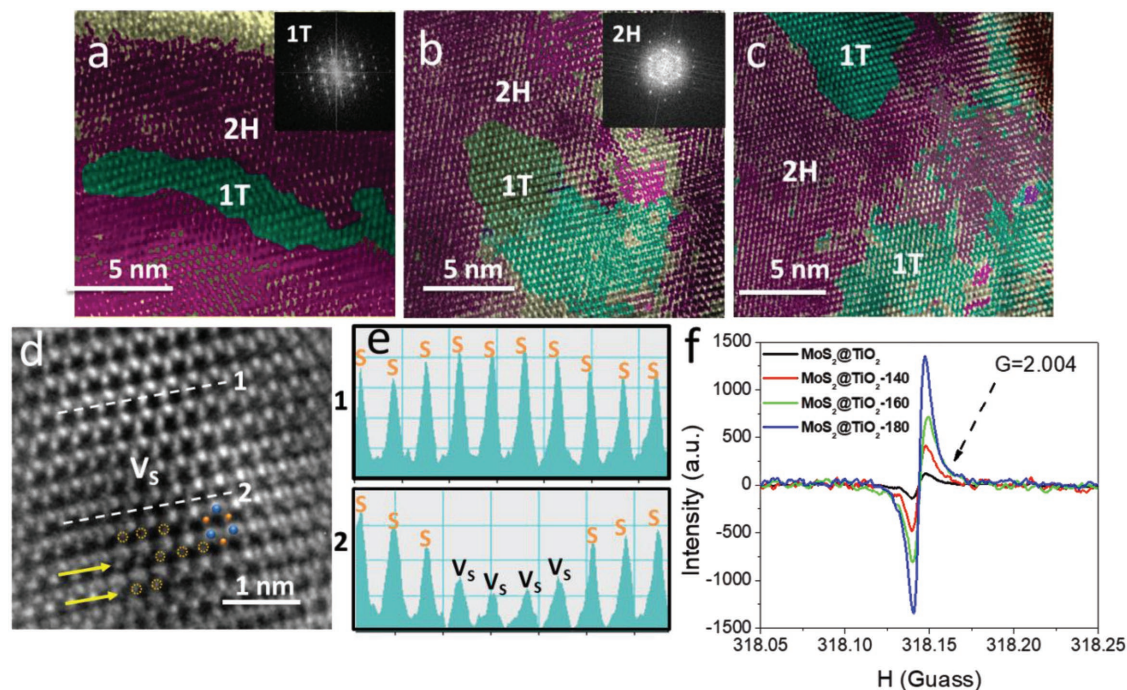

Figure 2. a–c) HRTEM images of $MoS_2@TiO_2$-140, $MoS_2@TiO_2$-160, and $MoS_2@TiO_2$-180, respectively. The insets show the corresponding FFT patterns converted from insets (a, b), representing 1T- and 2H-phases, respectively. d) Atomic-resolution HAADF-STEM of $MoS_2@TiO_2$-140 with S atom depletion area observed with weaker contrast (yellow arrows and dash circles). e) Brightness profiles along the dotted lines in inset (d) with a comparison of perfect atomic arrangement and S-depleted area. f) EPR spectra of $MoS_2@TiO_2$ before and after hydrothermal treatment, reflecting the significant increase in the number of V_S.

ADVANCED
SCIENCE NEWS
www.advancedsciencenews.com

ADVANCED
OPTICAL
MATERIALS
www.advopticalmat.de

increases continuously with consuming 2H-MoS$_2$ (violet color) by increasing temperature. The corresponding selected area FFT patterns of 2H-MoS$_2$ and 1T-MoS$_2$ are inserted at the right up corner of Figure 2a,b, respectively. Raman spectrum (Figure S5b, Supporting Information) was also used to study the phase transition of MoS$_2$ caused by hydrothermal treatment. The prominent Raman peaks at 381 and 407 cm^{-1} are assigned to the characteristic in-plane E$^1_{2g}$ and out-of-plane A$_{1g}$ vibration modes of 2H-MoS$_2$, respectively. No other peaks can be found in the samples hydrothermally treated at 120 °C, implying the pure 2H phase of the sample. At higher temperatures (140–180 °C), additional Raman peaks are identified at 200, 226, and 355 cm^{-1}, attributing to 1T-MoS$_2$.[19] The Raman shift difference between E$^1_{2g}$ and A$_{1g}$ modes decreases monotonically from 25.1 to 22.9 cm^{-1} with increasing hydrothermal temperature, indicating the decrease of the stacking layer number from 10 to 3.[20] Besides the hydrothermal temperature, the hydrothermal duration also affects the phase transition of MoS$_2$. When the reaction time is prolonged to 24 h at 180 °C, Raman peaks of 2H-MoS$_2$ appear along with the disappearance of 1T-MoS$_2$ (Figure S5c, Supporting Information). Furthermore, an extended hydrothermal duration at other temperatures (180 °C–36 h, 200 °C–12 h, and 200 °C–24 h) even reveals the amorphization of MoS$_2$. Coupled with SEM results (Figure S6a–c, Supporting Information), it can be concluded that a proper hydrothermal temperature or reaction time could promote the formation of 1T-MoS$_2$ NFs on the materials surface, forming a hybrid core–shell architecture composed of 2H-MoS$_2$ in the core and 1T-MoS$_2$ on the shell. However, a higher temperature and longer duration will degrade the crystal MoS$_2$ into an amorphous structure.

X-ray photoelectron spectroscopy (XPS) was used to quantify the content of 1T-MoS$_2$ in the heterostructured catalysts (Figure 3a; Figure S7, Supporting Information). The coexistence of MoS$_2$ and TiO$_2$ in the samples was confirmed by XPS survey scan (Figure S7a, Supporting Information). The XPS peaks of Ti and O are corroborated by the crystalline TiO$_2$ reported previously (Figure S7b,c, Supporting Information).[17] Two binding energy of S 2p (Figure S7d,e, Supporting Information) at 161.7 and 163.2 eV are assigned to the lattice S^{2-} in MoS$_2$. The upshifted peak at 169.3 eV is due to the existence of Mo–O–S bonds or oxidized S on the surface of MoS$_2$.[13a] The percentage of 1T-MoS$_2$ is estimated by fitting the high-resolution Mo 3d spectra. Based on the ground-state energy variation of 2H- and 1T-MoS$_2$ (0.8 eV), a pair of doublets at 229.4/232.8 and 228.7/232.1 eV are fitted, corresponding to the Mo 3d$_{3/2}$ and Mo 3d$_{5/2}$, respectively (Figure 3a).[13b,21] According to the assigned doublet of 1T-MoS$_2$ (228.7/232.1 eV), the percentage of 1T-MoS$_2$ in the hybrid catalysts is determined to be 7.0%, 27%, 44%, and 53% for MoS$_2$@TiO$_2$, MoS$_2$@TiO$_2$-140, MoS$_2$@TiO$_2$-160, and MoS$_2$@TiO$_2$-180, respectively (Table S1, Supporting Information). Besides the phase engineering, hydrothermal treatment also creates the V_S on the edges of MoS$_2$, which acts as active sites for catalytic reactions.[16] The formation of defect sites (V_S) in the hydrothermally treated MoS$_2$ was observed in MoS$_2$@TiO$_2$-140 by HAADF-STEM (Figure 2d), as marked by the yellow dashed circles and arrows.[22] The V_S exhibits local "staging" structures, as seen from most S atoms throughout the layers and linear brightness profiles along the S atoms in the crystal lattice (along with the dashed line 1 and 2 in Figure 2d,e). Electron paramagnetic resonance (EPR) was used to quantitatively measure the unsaturated defects in MoS$_2$@TiO$_2$ before and after hydrothermal treatment (Figure 2f). By integrating the enhanced characteristic signal at $g = 2.004$, the numbers of the exposed V_S in MoS$_2$@TiO$_2$-140, MoS$_2$@TiO$_2$-160, and MoS$_2$@TiO$_2$-180 are estimated to be three, four, seven
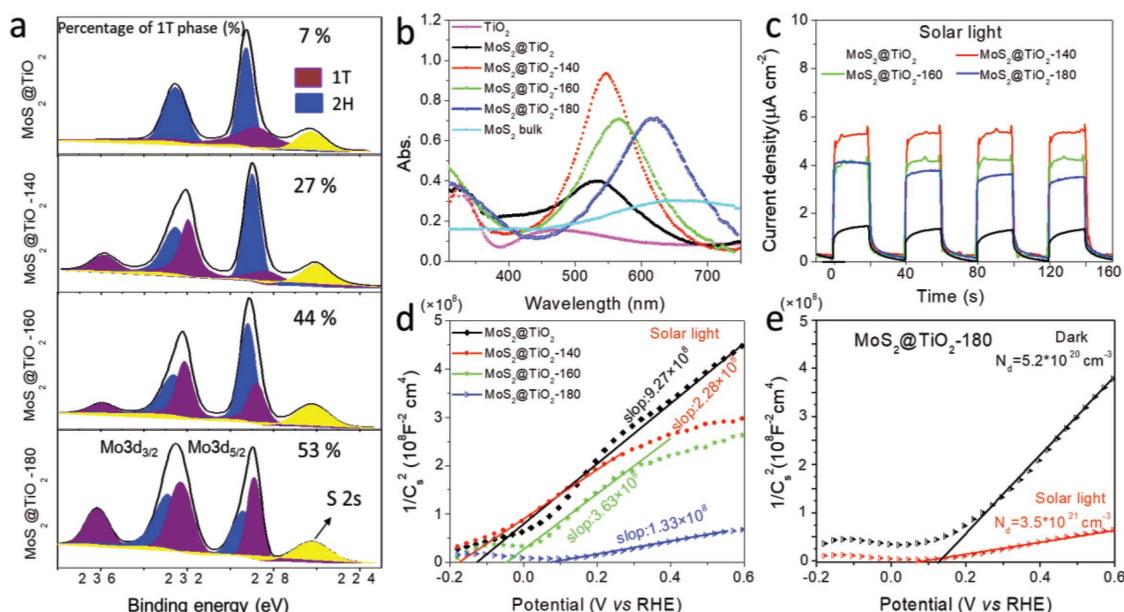
Figure 3. a) Mo3d XPS spectra of the as-prepared MoS$_2$@TiO$_2$ and the hydrothermally treated samples as a function of hydrothermal temperature (fitted by the binding energy variation of 1T- and 2H-phase). b,c) UV–vis diffuse reflectance spectra of the samples and the corresponding transient photocurrent responses under the simulated solar light. d) Mott–Schottky plots of MoS$_2$@TiO$_2$ hydrothermally treated at different temperatures and e) the curve comparison in dark and solar light for the MoS$_2$@TiO$_2$-180.

times that of the pristine $MoS_2@TiO_2$. It infers that a large number of dangling bonds are created in the hydrothermal process. The amount of V_S was also confirmed by the inductively coupled plasma method (ICP, Table S1, Supporting Information). The S/Mo ratio decreases from 1.97 to 1.80 after hydrothermal treatment at different temperatures, suggesting a tunable V_S concentration in a range of 1.5%–10%. It is found that the amount of V_S corresponds with the 1T phase in the samples. V_S is considered to be mainly responsible for crystal asymmetry of MoS_2, where electronic structures are changed slightly.[18] Photogenerated electrons in a higher Fermi level are easy to transfer to the unoccupied vacancies on the surface of MoS_2. When the orbital density vibration of these electrons resonant with incident light, photoinduced local dipoles and charge separation is generated and a confined local field can be formed around MoS_2 surface. The V_S leads to the LSPR effects in this work. Second, $1T-MoS_2$ is determined to be more active than $2H-MoS_2$ during catalytic reactions by the metallic property and superior conductivity.[14] However, $1T-MoS_2$ is unstable at room temperature and intends to transfer back to $2H-MoS_2$. Here, the V_S and charged "hot" electrons are helpful to fix the 1T phase during storage and photocatalysis. To summarize, the V_S in MoS_2 nanoflakes is the essential role in both the visible light absorption by LSPR and reaction kinetics during photocatalysis.

UV–vis diffuse reflectance spectra (Figure 3b) and transient photocurrent response under simulated solar light (Figure 3c) were used to analyze the photoresponse of the materials. A control sample was fabricated by sulfurizing Mo foil. The obtained MoS_2 NFs with a size of 100 nm agglomerate together and form flower-like clusters (Figure S2f (Supporting Information), denoted as MoS_2-bulk). As shown in the absorption spectra (Figure 3b), the TiO_2 substrate exhibits a typical UV light absorption with a band edge at 360–380 nm. While the MoS_2-bulk shows a broad photoresponse peak at 650 nm, ascribed to the bandgap excitation of MoS_2. Notably, a slight bandgap narrowing of TiO_2 (from 3.3 to 3.1 eV; band edge: 400 nm) is revealed in the $MoS_2@TiO_2$ heterostructures, which may be derived from the strain-induced band structure modifications at the TiO_2/MoS_2 interface.[23] Moreover, a strong peak at about 550 nm was observed in the visible region after forming the $MoS_2@TiO_2$ heterostructures due to the LSPR-induced light absorption.[8] As compared to the pristine $MoS_2@TiO_2$, the exfoliated samples ($MoS_2@TiO_2$-140, $MoS_2@TiO_2$-160, and $MoS_2@TiO_2$-180) show much bigger extinction cross section in the wavelength range of 450–700 nm. The photoresponse peak redshifts from 540 to 560 and 630 nm when the hydrothermal temperature increases from 140 to 160 °C and 180, respectively. High free carrier concentration on the MoS_2 surface is considered to be a vital factor to boost the LSPR, which is closely associated with the phase composition of MoS_2 and vacancy sites. Surface vacancies on the hydrothermally treated MoS_2 serve as charged centers, where active electrons can be localized and collide with external photons, thus resulting in the enhanced LSPR.[24] In addition, the phase transition to the metallic $1T-MoS_2$ (verified by the TEM, Raman, and EPR results) also contribute to the metal-like LSPR behavior. Traditionally, the central resonance frequency (ω_{LSPR}) of the semiconductor is size-dependent. A smaller NC leads to a blue-shift of the

light absorption peak.[13a,25] However, an inverse tendency was observed in the optical measurements of $MoS_2@TiO_2$ (peak wavelength: $MoS_2@TiO_2$-140 < $MoS_2@TiO_2$-160 < $MoS_2@TiO_2$-180), which may be caused by the free carrier energy loss on the MoS_2 NFs.[8,26] Because the amorphous MoS_2 surface serves as the optical scattering centers, leading to the reduction of free carrier energy. Therefore, a redshift of light absorption peak was observed in the sample with a thicker defective surface layer (Equations S4-S6 in Supporting Information).[6,8]

To validate the aforementioned assumption, the Mott–Schottky analysis was conducted on the pristine $MoS_2@TiO_2$ and hydrothermally treated samples at a frequency of 5 kHz in both dark and simulated solar light environment (Figure 3d,e). As expected, all the samples are n-type semiconductors with the positive slope for the curves. The calculated carrier concentrations (N_d) and flat-band potential (E_f) of the heterostructures are listed in Table S2 in Supporting Information. Evidently, the exfoliated $MoS_2@TiO_2$ has a significantly enhanced carrier density than the pristine one, particularly for the $MoS_2@TiO_2$-180 (3.5×10^{21} cm^{-3}). This enhanced donor density is essentially due to the increment of the V_S and sufficient charged centers on the sample surface. However, the $MoS_2@TiO_2$-140 shows a more negative Fermi level (–0.17 V vs RHE) than the $MoS_2@TiO_2$-160 (–0.05 V vs RHE) and $MoS_2@TiO_2$-180 (0.07 V vs RHE). This indicates an upward shift electronic energy of the plasmonic electrons in the $MoS_2@TiO_2$-140. As a supplementary evidence, the time-dependent photocurrent density (Figure 3c, in 0.5 M $NaSO_4$ solution at a bias of 0.4 V vs RHE) of $MoS_2@TiO_2$-140 is identified to be stronger than that of other samples. The charge carrier density comparison of these catalysts under dark and solar light illumination (Figure 3e) further prove the supreme activity of the sample upon solar light excitation.

The photocatalytic H_2 evolution performance of the $MoS_2@TiO_2$ heterostructures was tested by measuring the time-dependent H_2 yield under simulated solar light irradiation (**Figure 4**a). The hydrothermally treated $MoS_2@TiO_2$ films present the prompt increases with the reaction time, indicating the enhanced activity after exfoliation of MoS_2. In particular, the $MoS_2@TiO_2$-140 exhibits the optimum H_2 evolution rate of 151 μmol h^{-1}, which is much better than the control samples (TiO_2, sulfurized TiO_2, and Mo-loaded TiO_2 films). A slight deteriorated performance was observed on the samples treated with higher hydrothermal temperatures (160 and 180 °C), caused by rapid recombination of photogenerated carriers on the samples with thicker surface amorphous layers. The normalized catalytic activities based on the geometric sample area are shown in Figure S8 in the Supporting Information. An optimal STH conversion rate of 308 μmol h^{-1} cm^{-2} is achieved on the $MoS_2@TiO_2$-140 heterostructure, which is superior to the state-of-the-art plasmonic catalysts (Table S3, Supporting Information). The plasmon-driven solar water splitting was explored by testing the H_2 evolution against the wavelength of incident light (cutting out from the simulated solar light, 400–700 nm, Figure 4c). The maximum H_2 evolution rates under monochromatic light irradiation were measured to be 48, 44, and 40 μmol h^{-1} for $MoS_2@TiO_2$-140, $MoS_2@TiO_2$-160, and $MoS_2@TiO_2$-180, respectively. And the optimal excitation wavelength is located within the region of 500–600 nm, which is in good agreement with the absorption spectra profile (Figure 3b).
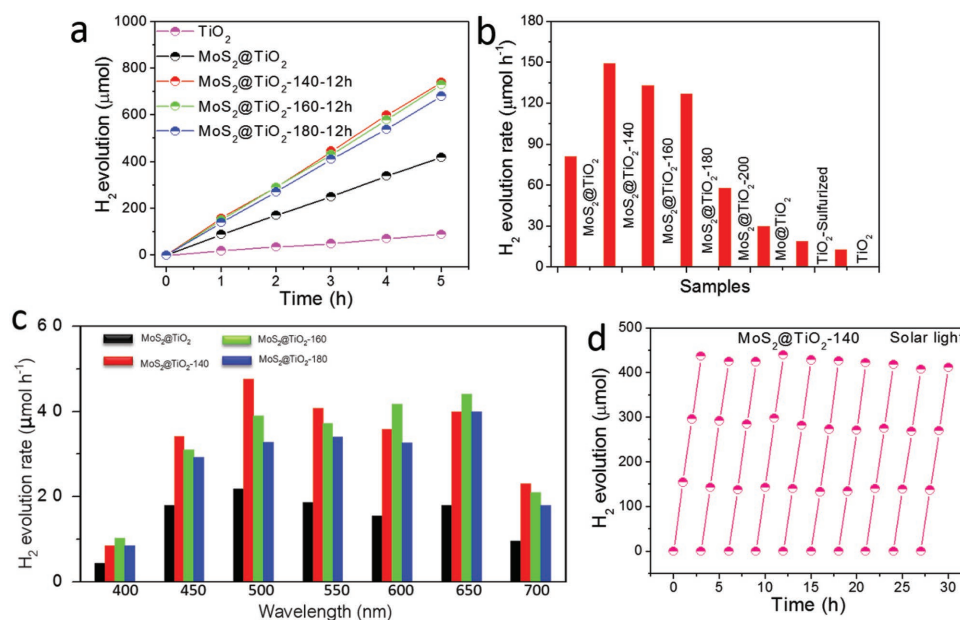
Figure 4. a,b) Time-dependent photocatalytic H_2 evolution of different samples and corresponding average H_2 yield rate. c) H_2 yield rate obtained under the monochromatic light (cutting out from the simulated solar light) irradiation from 400–700 nm with 50 nm interval. d) Recycling performance of $MoS_2@TiO_2$-140 in 30 h of continuous reaction.

The pristine TiO_2 film itself is catalytically inactive for H_2 evolution under visible light irradiation. The LSPR-excitation of the $MoS_2@TiO_2$ heterostructure provides the main driving force for the solar water reduction, which can be improved through the suggested phase-/defect-engineering. To study the stability of 1T-MoS_2, the $MoS_2@TiO_2$-140 was irradiated over 30 h under H_2 evolution conditions for ten continuous cycles (Figure 4d). Almost 90% of the incipient activity was maintained after 30 h testing, indicating the very stable 1T-MoS_2. A considerably deteriorated H_2 evolution was found on the control sample of MoS_2-bulk due to the nanoflake shedding effect (Figure S9, Supporting Information). It indicates that the periodic TiO_2 nanocavities not only contribute to UV-light absorption but also serve as a host to stabilize the 1T-MoS_2 NFs in the heterostructures.

The EM field distribution was simulated by a finite element method (FEM, **Figure 5**a). A single TiO_2 nanocavity loaded with MoS_2 was used as a model in the simulation (Figure S10, Supporting Information). By modulating the dielectric constant of the phase-/defect-engineered MoS_2, a strong EM enhancement is formed at the tip of MoS_2 via coupling the light irradiation (500 nm) with LSPR. The most enhanced EM field is generated on the hydrothermally treated MoS_2 (Figure 5a₁) with more active sites and overlapped EM field distribution between MoS_2 NFs, leading to an improved photocatalytic H_2 production. The hot electrons transfer pathway of $MoS_2@TiO_2$ (Figure 5b) follows the classical catalytic process in the plasmonic metal/TiO_2 heterostructure.[27] The hot electrons at the vicinity of MoS_2 either directly transfer to the conduction band (CB) of TiO_2 or indirectly relax to the CB of MoS_2 and then further transfer to TiO_2. The band structure arrangement of "plasmonic electrons—CB of MoS_2—CB of TiO_2" results in a suppressive recombination of hot electrons and promotes photocatalytic activity for H_2 evolution. Besides the plasmonic effect, the intrinsic excitations of MoS_2 and TiO_2 also contribute to the photogenerated electrons and H_2 evolution. Herein, the periodic TiO_2 nanocavities seamlessly laminated with MoS_2 NFs show a drastically reduced charge barrier, resulting in a lower resistance and suppressed quenching during the solar H_2 evolution.
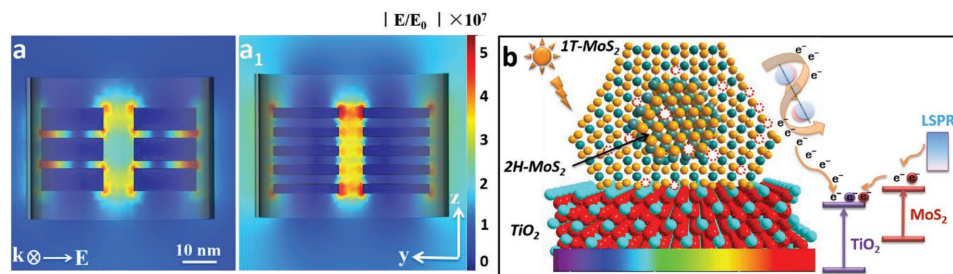
Figure 5. a–a₁) FEM simulation of the near-field electric field distribution in the $MoS_2@TiO_2$ heterostructures excited by a 500 nm laser (a: pristine $MoS_2@TiO_2$, a₁: hydrothermally treated $MoS_2@TiO_2$). b) Schematic diagram showing the energy band structure and electrons transfer for H^+ reduction.

Typically, the 1T-MoS_2 is metastable and will transform back to the 2H-MoS_2 after storing in an open-air for a while.[14] To examine the stability of the 1T-phased MoS_2 in the heterostructure, time-dependent Raman spectra of $MoS_2@TiO_2$-140 were measured in 120 d with an interval of 30 d for each measurement (Figure S11, Supporting Information). The photon modes of E^1_{2g} and A_{1g}, corresponding to 2H-MoS_2 (marked with black squares), were observed in all the spectra. Additional vibration modes belonging to 1T-MoS_2 (marked with asterisks) were detected from the spectra in the initial 60 d, which gradually reduces accompanied by an increase in A_{1g} peak. On the contrary, the Raman analysis on the MoS_2-bulk shows that the 1T-MoS_2 disappears quickly within 30 d. This suggests that the periodic TiO_2 nanocavities and defect-engineered characteristic play great roles in stabilizing the 1T-MoS_2 for long-term utilization. For the $MoS_2@TiO_2$-140 heterostructure, after performing continuous solar H_2 evolution tests (3 h per test, Figure 4d), the XPS peaks of Mo 3d show no change, indicating the stable 1T-MoS_2 in the heterostructures (Figure S12a, Supporting Information). The Raman spectrum shows that the 1T-MoS_2 stay perfectly after 30 h testing (Figure S12b, Supporting Information).

In summary, phase-/defect-engineered $MoS_2@TiO_2$ catalysts were rationally designed in order to enhance the plasmonic effect for solar H_2 evolution. Particularly, after a hydrothermal treatment in $NaBH_4$ solution, the plasmonic resonance of MoS_2 has been significantly strengthened. The phase transition from 2H- to 1T-MoS_2 induced by the hydrothermal treatment coupled with the surface V_S are responsible for the enhanced LSPR, leading to a superior H_2 yield rate of 308 µmol h^{-1} cm^{-2}. Simulation studies (FEM) indicate that the significantly improved catalytic activity of the phase-/defect-engineered $MoS_2@TiO_2$ comes from the greatly enhanced EM filed and H^+ reduction dynamics. This work offers an innovative strategy to explore plasmonic catalysts with low cost and long-term durability for renewable energy future.

Supporting Information

Supporting Information is available from the Wiley Online Library or from the author.

Conflict of Interest

The authors declare no conflict of interest.

[1] a) Y. Yang, H. Fei, G. Ruan, Y. Li, J. M. Tour, *Adv. Funct. Mater.* **2015**, *25*, 6199; b) J. B. Priebe, J. Radnik, A. J. J. Lennox, M. M. Pohl, M. Karnahl, D. Hollmann, K. Grabow, U. Bentrup, H. Junge, M. Beller, *ACS Catal.* **2015**, *5*, 2137.

[2] M. Altomare, N. T. Nguyen, S. Hejazi, P. Schmuki, *Adv. Funct. Mater.* **2018**, *28*, 1704259.

[3] a) D. N. Pei, G. Li, A. Y. Zhang, Z. Xing, J. J. Chen, M. Yang, H. Q. Yu, *Nat. Commun.* **2015**, *6*, 8696; b) A. Polman, K. R. Catchpole, *Opt. Express* **2008**, *16*, 21793.

[4] a) S. Kment, F. Riboni, S. Pausova, L. Wang, L. Wang, H. Han, Z. Hubicka, J. Krysa, P. Schmuki, R. Zboril, *Chem. Soc. Rev.* **2017**, *46*, 3716; b) L. J. Zhang, S. Li, B. K. Liu, D. J. Wang, T. F. Xie, *ACS Catal.* **2014**, *4*, 3724; c) H. Wang, R. P. Liu, Y. T. Li, X. J. Lu, Q. Wang, S. Q. Zhao, K. J. Yuan, Z. M. Cui, X. Li, S. Xin, R. Zhang, M. Lei, Z. Q. Lin, *Joule* **2018**, *2*, 337.

[5] a) Z. Zhang, J. Huang, Y. Fang, M. Zhang, K. Liu, B. Dong, *Adv. Mater.* **2017**, *29*, 1606688; b) H. Cheng, X. Qian, Y. Kuwahara, K. Mori, H. Yamashita, *Adv. Mater.* **2015**, *27*, 4616.

[6] X. Zhang, Y. L. Chen, R. S. Liu, D. P. Tsai, *Rep. Prog. Physics* **2013**, *76*, 046401.

[7] a) N. T. Nguyen, M. Altomare, J. Yoo, P. Schmuki, *Adv. Mater.* **2015**, *27*, 3208; b) H. J. Yang, L. Geng, Y. T. Zhang, G. Chang, Z. L. Zhang, X. Liu, M. Lei, Y. B. He, *Appl. Surf. Sci.* **2019**, *466*, 385.

[8] A. Agrawal, S. H. Cho, O. Zandi, S. Ghosh, R. W. Johns, D. J. Milliron, *Chem. Rev.* **2018**, *118*, 3121.

[9] a) A. N. Grigorenko, M. Polini, K. S. Novoselov, *Nat. Photonics* **2012**, *6*, 749; b) P. Wang, W. Zhang, O. Liang, M. Pantoja, J. Katzer, T. Schroeder, Y. H. Xie, *ACS Nano* **2012**, *6*, 6244.

[10] C. Tan, Z. Luo, A. Chaturvedi, Y. Cai, Y. Du, Y. Gong, Y. Huang, Z. Lai, X. Zhang, L. Zheng, X. Qi, M. H. Goh, J. Wang, S. Han, X. J. Wu, L. Gu, C. Kloc, H. Zhang, *Adv. Mater.* **2018**, *30*, 1705509.

[11] K. Chang, Z. Mei, T. Wang, Q. Kang, S. Ouyang, J. Ye, *ACS Nano* **2014**, *8*, 7078.

[12] Y. Yin, P. Miao, Y. Zhang, J. Han, X. Zhang, Y. Gong, L. Gu, C. Xu, T. Yao, P. Xu, *Adv. Funct. Mater.* **2017**, *27*, 1606694.

[13] a) L. Guo, Z. Yang, K. Marcus, Z. Li, B. Luo, L. Zhou, X. Wang, Y. Du, Y. Yang, *Energy Environ. Sci.* **2017**, *11*, 106; b) L. Wang, X. Liu, J. Luo, X. Duan, J. Crittenden, C. Liu, S. Zhang, Y. Pei, Y. Zeng, X. Duan, *Angew. Chem., Int. Ed.* **2017**, *56*, 7610.

[14] D. Y. Hwang, K. H. Choi, D. H. Suh, *Nanoscale* **2018**, *10*, 7918.

[15] Y. Kang, S. Najmaei, Z. Liu, Y. Bao, Y. Wang, X. Zhu, N. J. Halas, P. Nordlander, P. M. Ajayan, J. Lou, *Adv. Mater.* **2014**, *26*, 6467.

[16] A. Jawaid, J. Che, L. F. Drummy, J. Bultman, A. Waite, M. S. Hsiao, R. A. Vaia, *ACS Nano* **2017**, *11*, 635.

[17] a) L. Guo, K. Liang, K. Marcus, Z. Li, L. Zhou, P. D. Mani, H. Chen, C. Shen, Y. Dong, L. Zhai, *ACS Appl. Mater. Interfaces* **2016**, *8*, 34970; b) K. Bi, M. H. Bi, Y. N. Hao, W. Luo, Z. M. Cai, X. H. Wang, Y. H. Huang, *Nano Energy* **2018**, *51*, 513; c) L. Guo, J. Deng, G. Wang, Y. Hao, K. Bi, X. Wang, Y. Yang, *Adv. Funct. Mater.* **2018**, *28*, 1804540.

[18] M. A. Lukowski, A. S. Daniel, F. Meng, A. Forticaux, L. Li, S. Jin, *J. Am. Chem. Soc.* **2013**, *135*, 10274.

[19] S. J. Sandoval, D. Yang, R. F. Frindt, J. C. Irwin, *Phys. Rev. B* **1991**, *44*, 3955.

[20] L. Liang, V. Meunier, *Nanoscale* **2014**, *6*, 5394.

[21] Y. Yin, Y. Zhang, T. Gao, T. Yao, X. Zhang, J. Han, X. Wang, Z. Zhang, P. Xu, P. Zhang, *Adv. Mater.* **2017**, *29*, 1700311.

[22] G. Liu, A. W. Robertson, M. J. Li, W. C. H. Kuo, M. T. Darby, M. H. Muhieddine, Y. C. Lin, K. Suenaga, M. Stamatakis, J. H. Warner, *Nat. Chem.* **2017**, *9*, 810.

[23] a) Y. Yang, C. Sun, L. Wang, Z. Liu, G. Liu, X. Ma, H. Cheng, *Adv. Energy Mater.* **2014**, *4*, 1400057; b) Z. Yu, X. Chen, X. Kang, Y. Xie, H. Zhu, S. Wang, S. Ullah, H. Ma, L. Wang, G. Liu, X. Ma, H. Cheng, *Adv. Mater.* **2018**, *30*, 1706259.

[24] M. Ye, D. Winslow, D. Zhang, R. Pandey, Y. K. Yap, *Photonics* **2015**, *2*, 288.

[25] A. Agrawal, I. Kriegel, D. J. Milliron, *J. Phys. Chem. C* **2015**, *119*, 6227.

[26] O. Zandi, A. Agrawal, A. B. Shearer, L. C. Gilbert, C. J. Dahlman, C. M. Staller, D. J. Milliron, *Nat. Mater.* **2018**, *17*, 710.

[27] Z. Zhang, L. Zhang, M. N. Hedhili, H. Zhang, P. Wang, *Nano Lett.* **2013**, *13*, 14.